Earth, Planets and Space

FULL PAPER

Open Access

On the detectability of the magnetic fields induced by ocean circulation in geomagnetic satellite observations

Aaron Hornschild[1*], Julien Baerenzung[1], Jan Saynisch-Wagner[1], Christopher Irrgang[1] and Maik Thomas[1,2]

Abstract

Due to their sensitivity to conductivity and oceanic transport, magnetic signals caused by the movement of the ocean are a beneficial source of information. Satellite observed tidal-induced magnetic fields have already proven to be helpful to derive Earth's conductivity or ocean heat content. However, magnetic signals caused by ocean circulation are still unobserved in satellite magnetometer data. We present a novel method to detect these magnetic signals from ocean circulation using an observing system simulation experiment. The introduced approach relies on the assimilation of satellite magnetometer data based on a Kalman filter algorithm. The separation from other magnetic contributions is attained by predicting the temporal behavior of the ocean-induced magnetic field through presumed proxies. We evaluate the proposed method in different test case scenarios. The results demonstrate a possible detectability of the magnetic signal in large parts of the ocean. Furthermore, we point out the crucial dependence on the magnetic signal's variability and show that our approach is robust to slight spatial and temporal deviations of the presumed proxies. Additionally, we showed that including simple prior spatial constraints could further improve the assimilation results. Our findings indicate an appropriate sensitivity of the detection method for an application outside the presented observing system simulation experiment. Therefore, we finally discussed potential issues and required advances toward the method's application on original geomagnetic satellite observations.

Keywords: Electromagnetic induction, Ocean circulation, Satellite magnetometer observations, Kalman filter, Assimilation, Observing system simulation experiment

*Correspondence: aaron.hornschild@gfz-potsdam.de

[1] Helmholtz Centre Potsdam, GFZ German Research Centre for Geosciences, Section 1.3: Earth System Modelling, Potsdam, Germany
Full list of author information is available at the end of the article

Graphical Abstract

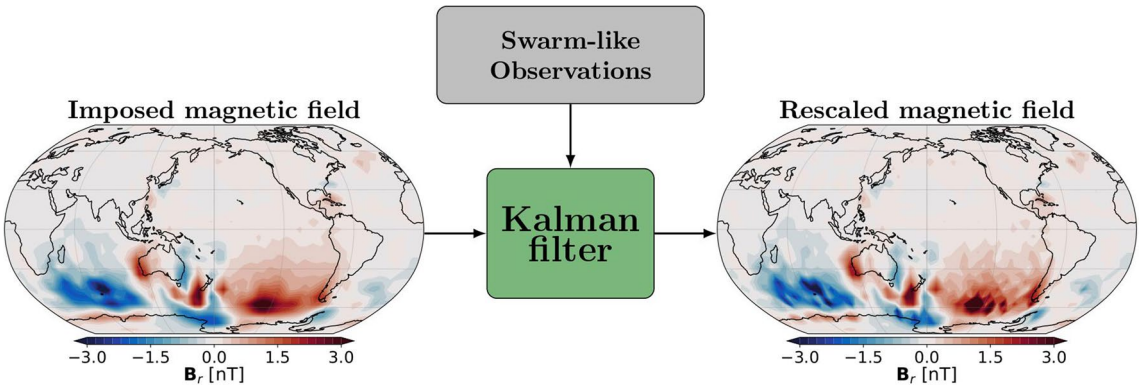

Introduction

The motion of conductive saltwater through the Earth's ambient magnetic field induces electric and magnetic fields. These electromagnetic induction processes in the ocean were the subject of various theoretical research studies (Larsen 1968; Sanford 1971). Typically one distinguishes between two types of ocean-induced magnetic fields (OIMF): the one associated with tidal motion and the one caused by ocean circulation. Several research activities were already dedicated to both tidal electromagnetic signals (e.g., Tyler et al. 2003; Dostal et al. 2012; Schnepf et al. 2014) as well as OIMF from circulation (e.g., Stephenson and Bryan 1992; Flosadottir et al. 1997; Tyler et al. 1997; Vivier et al. 2004; Manoj et al. 2006; Irrgang et al. 2016, 2017, 2018).

Of particular importance is the dependence of these induced electromagnetic fields on electric conductivity and transport in the ocean and the electromagnetic structure in the Earth. Primarily because the poloidal secondary magnetic field can reach outside the ocean, the radial component of OIMF provides a remote observation possibility. For this reason, oceanic electromagnetic signals are an exciting source of indirect observation. Consequently, many additional research activities addressed ocean-induced magnetic signals, covering a broad spectrum of topics. For example, Schnepf et al. (2015) and Grayver et al. (2016) used tidal magnetic signals to explore characteristics of the Earth structure; Saynisch et al. (2016) used the sensitivity on the electric conductivity to investigate the impact of climate variability; Petereit et al. (2018) analyzed the El Niño Southern Oscillation; and Irrgang et al. (2019) estimated the ocean heat content from magnetometer satellite observations.

Furthermore, OIMF gained increased interest since the beginning of the satellite era and high-precision magnetometer missions, like CHAMP and Swarm. But using magnetometer observations always requires a separation of the oceanic magnetic component from other parts of the geomagnetic field. Due to the small magnitude of OIMF compared to other magnetic contributions, this is a challenging task, especially for signals arising from ocean circulation. Regarding this separation, there is a clear advantage for the tidal OIMF due to the well-known temporal behavior of oceanic tides. Tyler et al. (2003) and Sabaka et al. (2016, 2018, 2020) could successfully extract the tidal magnetic signals from CHAMP and Swarm satellite data. However, up to now, OIMF from oceanic circulation could not be identified in satellite data. Not only was a successful separation not realized yet, but there is also a lack of ideas on how to achieve this (Kuvshinov 2008). Therefore, we propose a novel method to identify the magnetic signals from ocean circulation in satellite data. This paper aims to present our ideas towards a possible detection method in an observing system simulation experiment (OSSE). For the essential part of separating the magnetic contributions, we used the Kalman filter method from Baerenzung et al. (2020). This assimilation uses a Bayesian approach and prior spatial and temporal correlations to distinguish the different magnetic contributions. A principal difficulty concerning the separation of OIMF from circulation, especially compared to OIMF from tides, is their complex temporal behavior due to the irregular ocean flow. Hence, the crucial aspect of the proposed method is to predefine the temporal behavior of the OIMF from circulation. Saynisch et al. (2018) already suggested to predict magnetic signals from circulation and to use these proxies for a fit on magnetometer data. Saynisch et al. (2018) also pointed out the possibility of constructing the proxy OIMF from independent observations like satellite altimetry. However, in the OSSE presented here, we decided to use ocean model data in the first place to derive magnetic signals from

circulation. Subsequently, we impose these proxy OIMF's to the Kalman filter to constrain the temporal behavior. Furthermore, we aim to determine a scale factor by the assimilation of magnetometer data so that the imposed field finally matches the observations as best as possible. In the OSSE presented here, this factor is considered as a measure of detectability in the first place. In future steps, this scale factor could also provide several opportunities for further analysis. As the induced magnetic signals are first-order proportional to conductivity-weighted and depth-integrated ocean velocities, the scale factor can be understood as a proportional factor related to conductivity or depth. Moreover, because the Bayesian approach allows access to uncertainties, one could also analyze it as a quality factor containing information on how well a given proxy can explain the observations.

In the next section, we describe the data and methodology used in this study. Firstly, we specify the ocean model data; secondly, introduce an appropriate electromagnetic induction framework to derive OIMF (Fig. 2) and finally explain our OSSE with the employed Kalman filter-based assimilation. Afterward, the subsequent section presents and discusses the result of different test case scenarios of our OSSE. In the end, we discuss the results of our experiments and provide some concluding remarks as well as propositions for future work.

Data and methodology

Global ocean model data

The calculations of the OIMF in this study rely on data from an ocean general circulation model (OGCM). We took the OGCM data from the Estimating the Circulation and Climate of the Ocean, Phase II (ECCO2) project (https://ecco.jpl.nasa.gov/drive/files/ECCO2/cube92_latlon_quart_90S90N). The ECCO2 model uses a Greens function approach to estimate the ocean state (Menemenlis et al. 2005) and is constrained by several in situ and remote observational data (Menemenlis et al. 2008). The optimized solution "cube92" was used for this study. The Jet Propulsion Laboratory provides this solution on a latitude–longitude grid with a spatial resolution of 0.25° degree and 50 depth levels. We reduced the spatial resolution by interpolation onto a 1° grid to calculate the OIMF. The 3D output fields of the ocean model has been provided as 3-day averages. We considered a data period of 7.1 years (from 2013.9 until 2021.0) corresponding to the Swarm satellite mission, which results in 865 timesteps. Our OIMF calculations made use of the four oceanic variables: zonal velocity (u), meridional velocity (v), temperature (T), and salinity (S). In general, in this paper, we refer to a coordinate system (x, y, z), where x indicates the zonal (eastwards), y the meridional (northwards), and z the radial direction (upwards).

Electromagnetic induction framework

The following section describes the procedure to obtain the radial magnetic field from the OGCM data. As stated before, the movement of conductive seawater through the Earth's magnetic field generates electric currents. Their corresponding density can be calculated using Ohm's law in combination with the Lorentz force, described by:

$$\vec{\mathbf{J}}_{\mathbf{imp}} = \sigma \cdot \left(\vec{\mathbf{U}} \times \vec{\mathbf{B}}_{\mathbf{earth}}\right), \tag{1}$$

where σ denotes the ocean conductivity, $\vec{\mathbf{U}}$ the ocean velocity vector, and $\vec{\mathbf{B}}_{\mathbf{earth}}$ the Earth's main magnetic field. The external imposed electric current density ($\vec{\mathbf{J}}_{\mathbf{imp}}$) causes secondary magnetic fields in the ocean. As we consider steady ocean flow, which results in a slow induction process, the quasi-stationary part of the Maxwell's equations describes the generation of OIMF, by the relations:

$$\text{i)} \quad \nabla \times \vec{\mathbf{E}} = i\omega\vec{\mathbf{B}}, \quad \text{ii)} \quad \nabla \times \vec{\mathbf{B}} = \mu_0\left(\vec{\mathbf{J}} + \vec{\mathbf{J}}_{\mathbf{imp}}\right). \tag{2}$$

These two equations express the relation between the magnetic ($\vec{\mathbf{B}}$) and the electric field ($\vec{\mathbf{E}}$) in the frequency domain under the appearance of the externally induced electric current density ($\vec{\mathbf{J}}_{\mathbf{imp}}$), whereby $\vec{\mathbf{J}}$ denotes the electric current density, μ_0 the vacuum permeability and ω the angular frequency resulting from the time factor $\exp(-i\omega t)$. In this study, we used the X3DG electromagnetic induction solver (Kuvshinov 2008) to obtain a numerical solution to these equations for the poloidal part of the OIMF, which can reach outside the ocean. X3DG is a carefully tested and already widely used electromagnetic induction solver (Kelbert et al. 2014; Šachl et al. 2019) that uses an iterative volume integral approach to solve the Maxwell's equations in the frequency domain. Apart from the electric source, X3DG also requires an appropriate description of a conductance model. Figure 1 illustrates the processing steps to obtain both required inputs for the X3DG induction solver, the electric source, and the conductance model. We performed this calculation of the radial OIMF via the X3DG solver for every time step of the ECCO2 data set in a nearly static regime. In order to compute the steady flow solution in the frequency domain, the period was set to a large value (10^{18} days) similar to Manoj et al. (2006).

First, we calculated a 3D ocean conductivity time series. Irrgang et al. (2016) showed that a realistic 3D ocean conductivity description is needed and that especially its spatial distribution and temporal variation influence the OIMF. Therefore, we used the Gibbs Seawater Oceanographic Toolbox from the Thermodynamic Equation of Seawater 2010 [TEOS-10, McDougall and Barker

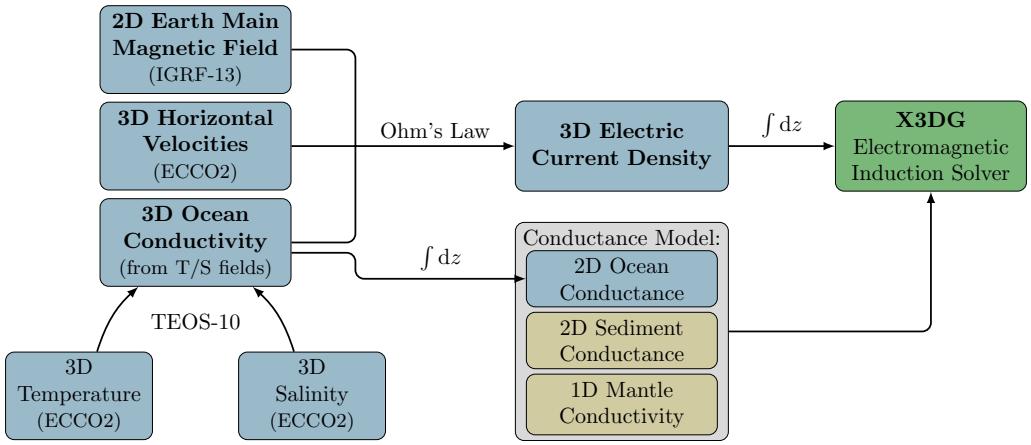

Fig. 1 Sketch of the processing steps for the input of the electromagnetic induction solver X3DG used in this study. Note: blue boxes highlight quantities, which are updated each time step

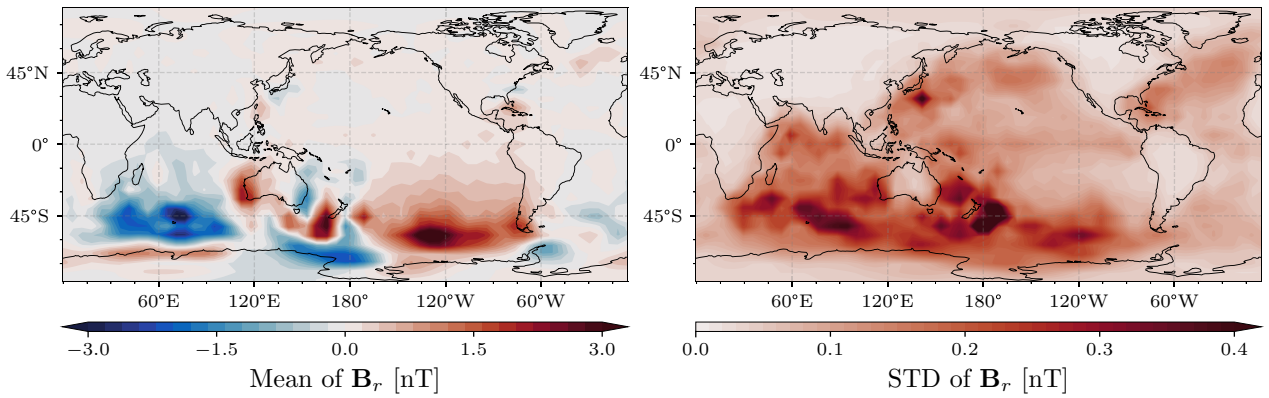

Fig. 2 Mean (left) and standard deviation (right) of the radial component of the magnetic field from ocean circulation (calculated from ECCO2 data) at sea surface height. The spatial resolution corresponds to a decomposition to spherical harmonic functions up to degree 30

(2011)] to derive 3D ocean conductivity from ECCO2 T/S fields and the pressure obtained from the depth [similar to Tyler et al. (2017)]. In this way, this study consistently relies on the ECCO2 dataset. In combination with the 3D time series of the ocean velocities from the ECCO2 model and the main magnetic field, Eq. 1 provides the 3D electric current density. Here, we assumed that vertical ocean velocities are negligible, resulting in an ocean velocity vector of $\vec{\mathbf{U}} = (u, v, 0)$. Furthermore, we took the Earth's main magnetic field data from the IGRF-13 model (Alken et al. 2021) and updated it for each time step to take secular variation into account (variations within ocean depth were neglected).

The conductance model consists of three parts: first, an ocean conductance layer, which stems from the 3D ocean conductivity by simple integration over depth. Second, a time constant sediment conductance layer. We computed this layer on a 1° grid with the heuristic approach from Everett et al. (2003) using the sediment thickness of Laske and Masters (1997). And third, a 1D mantle conductivity profile from Grayver et al. (2017), including a highly conductive core.

After all, this electromagnetic induction framework results in time series of radial 2D OIMF corresponding to the ECCO2 data set. Figure 2 shows the mean and the standard deviation (STD) of the calculated magnetic field from circulation over 7.1 years.

OSSE and Kalman filter-based assimilation

The main goal of this paper is to introduce a new detection method of ocean magnetic induced fields based on the assimilation of geomagnetic satellite observations. To this end, we used the Kalman filter algorithm, which has been already successfully used to derive the geomagnetic field model Kalmag (Baerenzung et al. 2020; Saynisch-Wagner et al. 2021). For our purpose, we added an

extra source accounting for the signal induced by ocean circulation to the algorithm. To extensively study the advantages and limitations of our approach, we developed an OSSE where real satellite magnetometer data are replaced by artificial ones.

To construct these artificial data, we first extracted the orbiting positions of the satellites Alpha and Bravo from the Swarm constellation between 2013.9 and 2021.0. In order to obtain a similar data distribution as the one used to derive the Kalmag model, the following selection was applied to this track set. The satellite positions were picked at a sampling rate of one every 10s, only nighttime locations were considered at low magnetic latitudes (below 60°), and the geomagnetic activity had to be low ($K_p \leq 2^0$). The second step of producing artificial observations consisted in generating realistic measurements. To do so, we simulated seven magnetic contributions, one associated with ocean circulation and six other, which are components of the Kalmag model and consist of a core field, a lithospheric field, an ionospheric field, and three magnetospheric fields (close, remote and fluctuating). Table 1 shows the maximum spatial resolution in spherical harmonics used for each components of the Kalmag model.

The spatio-temporal behaviors of the these contributions are prescribed by autoregressive processes (ARPs), as detailed in Baerenzung et al. (2020). Therefore, it is possible to generate some random time series for each of these sources. The initial state of these time series was randomly drawn from the ensemble of the Kalmag model in 2013.9 and then propagated with a time step of 30 min accordingly to the associated ARPs until 2021. Finally, at each time step, these sources are evaluated as vector field components at the current satellites' locations. To incorporate the oceanic contribution to the artificial measurements, we used the OIMF derived from the ECCO2 data as described in the previous section. The 865 snapshots of the OIMF were first converted in spherical harmonic functions (SH) up to degree of 30 using SHtools (Wieczorek and Meschede 2018) and then again evaluated at the different satellite positions. In our OSSE, this oceanic contribution, as well as the other randomly generated fields, correspond therefore to the true solutions we wish to recover with our assimilation algorithm.

Table 1 The six magnetic sources simulated by the Kalmag model and their used spatial resolution

Internal sources	SH degree	External sources	SH degree
Core field	20	Close magnetospheric field	10
Lithospheric field	75	Remote magnetospheric field	1
Ionospheric field	5	Fluctuating magnetospheric field	1

After the generation of artificial observations is completed, their assimilation can be initiated. We performed this operation using a Kalman filter algorithm which works in two alternating steps: first, a forecast step, where the spatio-temporal evolution of each magnetic source is predicted until some observations become available. Then an analysis step, where a Bayesian inversion updates the model accordingly to the data. The Bayesian approach allows not only to determine the mean-field, but also its associated uncertainties. The separation within the assimilation requires prior spatial and temporal characterizations of each magnetic source. For the non-oceanic contributions, this is realized with the autoregressive processes previously mentioned (see Baerenzung et al. 2020); whereas, for the oceanic contribution, our strategy is to calculate the OIMF from circulation in parallel to the Kalman filter algorithm and use the assimilation to determine a scale factor for these presumed proxies. Through this factor, we will be able to assess the detectability (whether the oceanic contribution can be extracted from the data or not) and, at a later stage, measure the quality of the a priori assumed OIMF (how well the data reflect these). Hence, in our OSSE, we can describe the relation between our presumed proxies of the OIMF (denoted as imposed oceanic field $\mathbf{B}_r^{\text{imposed}}$) and the oceanic magnetic contribution in the observations (denoted as true oceanic field $\mathbf{B}_r^{\text{true}}$) by the following expression:

$$\mathbf{k}(x,y) \cdot \mathbf{B}_r^{\text{imposed}}(t,x,y) \approx \mathbf{B}_r^{\text{true}}(t,x,y). \tag{3}$$

Consequently, the objective of the assimilation is to determine the local scale factor or detectability factor $\mathbf{k}(x,y)$. We chose to implement this as follows: first, the radial imposed oceanic magnetic field is projected on a grid of the Earth's surface and point-wise modulated by scale factor from the assimilation k^i on each grid point i, described by:

$$b_r^i = k^i \cdot b_r^{\text{imposed},i}, \tag{4}$$

where b_r^i denotes the radial magnetic field on the corresponding grid point i. Using a Gauss–Legendre grid (containing $N = (\ell_{\max}+1)\cdot(2\ell_{\max}+1)$ points) enables us to convert the radial magnetic field into a potential ϕ in the spherical harmonics domain through the following relation:

$$\phi_{\ell,m} = \sum_{i=1}^{N} b_r^i \omega^i P_{\ell,m}^i, \tag{5}$$

where the superscript i indicates the ith Gauss node of the grid, $P_{\ell,m}$ the associated Legendre polynomials of degree ℓ and order m, ω the Gauss weight, and $\phi_{\ell,m}$ describes the potential expanded up to SH of degree $\ell = \ell_{\max}$. The potential $\phi_{\ell,m}$ allows evaluating the predicted oceanic induced field everywhere above the Earth's surface, particularly at the different satellite positions, which is required to perform the analysis of the Kalman filter algorithm.

A scheme of the presented OSSE is displayed in Fig. 3. In this study, we also use the ECCO2 data to derive the imposed magnetic field. First of all, we investigate the case of $\mathbf{B}_r^{\text{imposed}} = \mathbf{B}_r^{\text{true}}$, if then the determined scale factor of the assimilation $\mathbf{k} = 1$, the Kalman filter algorithm's predictions at satellite locations correspond exactly to the oceanic contribution in the artificial observations. Therefore, we evaluate the detectability of the oceanic induced field in satellite magnetometer data by starting with an ensemble of $\mathbf{k} \neq 1$ and observing the convergence of $\mathbf{k}$'s ensemble mean value and associated standard deviation. In our experiments, we typically start with $\mathbf{k}(x, y)$ characterized on each grid point by the Gaussian distribution $\mathcal{N}(0, 1)$.

In a further step, we test another prior setup by imposing additional spatial information. So far, the scale factors at each grid were uncorrelated. However, it is reasonable to assume that nearby factors are not independent from one another. Both the spatial expansion of magnetic fields as well as a possible relation of the scale factor to oceanic quantities suggest a spatial correlation among the local scale factors. The Kalman filter algorithm allows us to incorporate such information via the parametrization of the prior covariance. Therefore, we decided to add a spatial correlation for the scale factors at the beginning of the assimilation. In the OSSE presented here, we initialized the assimilation with a prior spatial covariance following the parametrization:

$$C_{ij} = \exp\left(-\frac{d_{ij}}{l}\right), \tag{6}$$

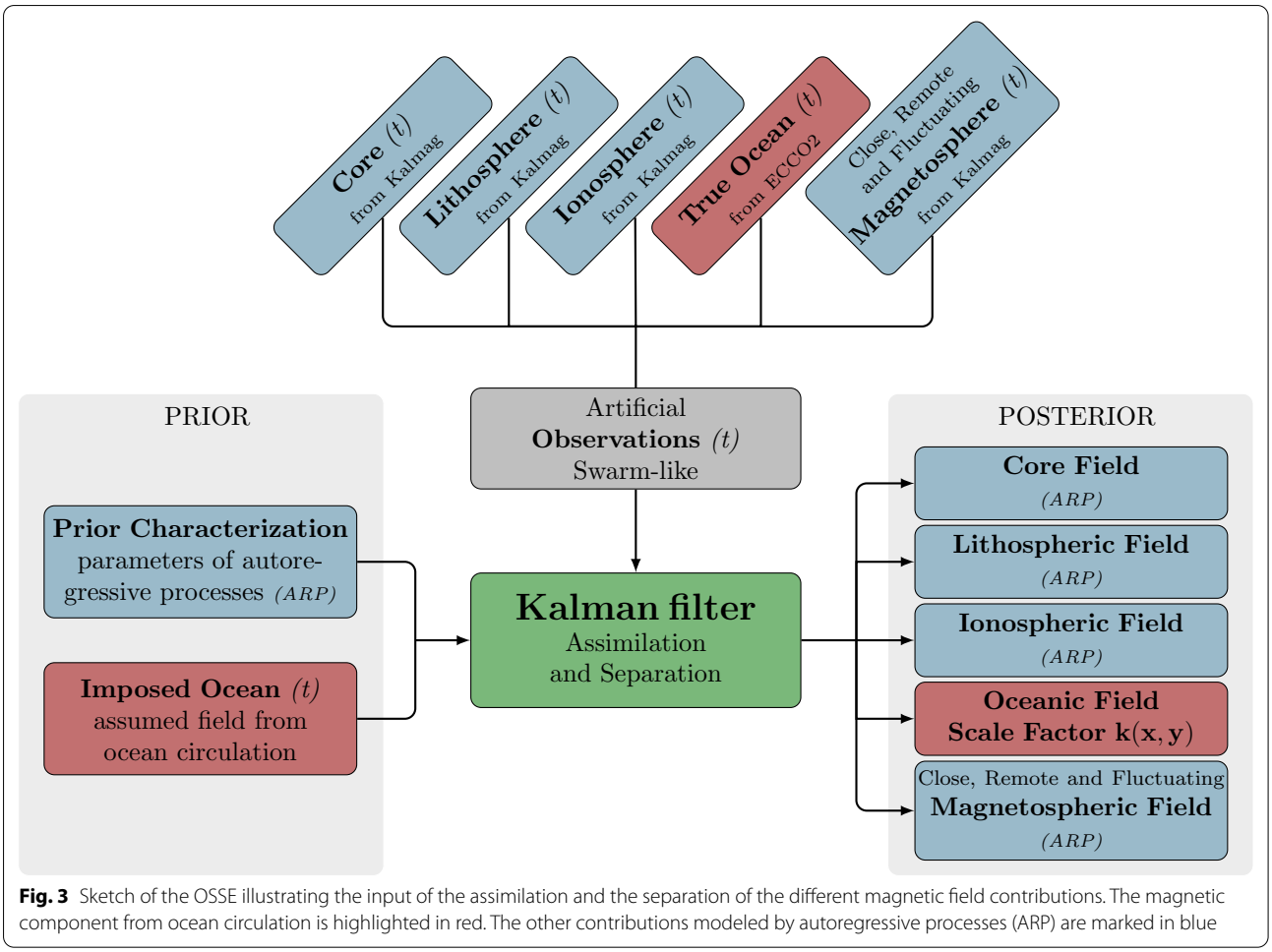

Fig. 3 Sketch of the OSSE illustrating the input of the assimilation and the separation of the different magnetic field contributions. The magnetic component from ocean circulation is highlighted in red. The other contributions modeled by autoregressive processes (ARP) are marked in blue

where i and j again indicate the Gauss node of the grid, and d_{ij} denotes the distance between two grid points. The covariance C_{ij} between two scale factors is assumed to exponentially decrease with distance compared to a characteristic correlation length scale l. When using exponential or gaussian covariance structures, the correlation length is typically a few times larger than the grid size (Brankart et al. 2010; Park et al. 2022). For example, the data assimilation experiment using OIMF by Irrgang et al. (2017) showed the best results with an observation radius of eight grid points. Here we chose a correlation length of 2000 km (which corresponds to ≈ 3.1 meridional grid points on the Gauss–Legendre grid). Such a characteristic length also matches with large-scale correlation lengths of oceanic quantities like oceanic heat (Mazloff et al. 2018) and salinity (Bao et al. 2020). Since there is no source of OIMF over land, the prior spatial correlation between scale factors is only applied between different grid points over the oceans (C_{ij} is set to zero for $i \neq j$ if i or j indicate a Gauss node located on land). To distinguish ocean and land grid points, we used the ETOPO1 dataset (Amante and Eakins 2009).

Our primary purpose here is to show that imposing a priori spatial correlations can improve the assimilation results. The following section presents the results of the OSSE for both cases without and with prior spatial correlations.

Results and discussion

We studied three test case scenarios in this paper. The main results are presented in a scenario with: *(A) identical true and imposed magnetic fields*, which means that the imposed proxies of the OIMF equal the true oceanic contribution in the observations. This case represents an ideal scenario, where the scale factor should be precisely one at each time step and each location (see Eq. 3). Imposing the exact OIMF from circulation may not be the most realistic scenario. However, it exhibits the general principle and the upper limit of our proposed method. Afterward, we present a second test case scenario with: *(B) deviating true and imposed magnetic fields*, which means that the imposed presumed proxies of the oceanic field slightly differ from true oceanic contribution in the observations. This second scenario is designed to examine the robustness and the optimality within the scale factor approach of our method and analyses the effect of these small deviations on the Kalman filter predictions. Within this study, we investigate the influence of spatial under-sampling and temporal smoothing of the presumed proxies on the scale factor determination. Finally, a third test case scenario is presented to show a possible application of the scale factor approach. This scenario uses a: *(C) deviating conductivity of the imposed magnetic field*, which means that the imposed proxies are calculated assuming a slightly different ocean conductivity.

For the analysis, the assimilation algorithm provides two types of quantities associated with the scale factor: the posterior mean and the posterior standard deviation of the ensemble of scale factors at each node of the Gauss–Legendre grid. We use the posterior mean $\mathbf{k}(x, y)$ as measure of OIMF detectability and consider its standard deviation $\sigma_{\mathbf{k}}(x, y)$ as the uncertainty of the scale factor. Note that the chosen distribution $\mathcal{N}(0, 1)$ of the scale factors at the beginning of the assimilation implies that the Kalman filter initially assumes no contribution from the OIMF. Under the influence of observations, the Kalman filter updates both the scale factor and its associated uncertainty, and through the assimilation of 7.1 years of Swarm-like artificial data, these quantities converge to their actual values. Eventually, the final determined scale factor $\mathbf{k}_f(x, y)$ (year 2021.0) is used to rescale the imposed OIMF:

$$\mathbf{B}_r^{\text{rescaled}}(t, x, y) = \mathbf{k}_f(x, y) \cdot \mathbf{B}_r^{\text{imposed}}(t, x, y). \tag{7}$$

Because at the beginning of the assimilation, no oceanic contribution was assumed, the rescaled field $\mathbf{B}_r^{\text{rescaled}}(t, x, y)$ reflects the detected OIMF and emphasizes the part of the signal gained from the true OIMF by the assimilation (under the given imposed field). Furthermore, the rescaled field is used to analyze the assimilation results. We utilize a normalized root mean square deviation (NRMSD) as a quality measure of how well the rescaled field reflects the true field, which is defined as follows:

$$\mathbf{NRMSD}(x, y) = \sqrt{\frac{\sum_{t_i=0}^{N} \left(\mathbf{B}_r^{\text{rescaled}}(t_i, x, y) - \mathbf{B}_r^{\text{true}}(t_i, x, y)\right)^2}{\sum_{t_i=0}^{N} \mathbf{B}_r^{\text{true}}(t_i, x, y)^2}}, \tag{8}$$

where t_i denotes the time steps and the normalization accounts for the relation of deviations to the strength of the true signal.

Test case scenario A: identical true and imposed magnetic field

In this scenario, the imposed oceanic field is identical to the true oceanic field included in the Swarm-like artificial data. This test case aims to demonstrate the main results, identify essential dependencies, and evaluate the determination of the scale factor. Since it is an idealistic scenario, it also serves as a reference. First, the results of the assimilation A.1 only using the imposed field as prior information for the oceanic source are presented. Subsequently, another improved assimilation result A.2 is shown, where prior spatial correlations are imposed to

enforce spatial constraints on the scale factor determination. Finally, assimilation A.3 is used to investigate the influence of the ionosphere on the method's sensitivity.

The first assimilation results A.1 obtained with a diagonal prior covariance matrix are presented in Fig. 4. The upper left plots show the final scale factor's deviation from the true value $\mathbf{k}_f = 1$ in this test case scenario. Note that in this ideal case, the deviation $|\mathbf{k}_f - 1|$ is equal to the NRMSD (see Eq. 8). The results show that the Kalman filter strongly reduces the deviation of the scale factor in nearly all oceanic areas. Expectedly, in large parts of the continental regions, where no magnetic signals from the ocean arise, the deviations of the scale factor remained close to the initial value of one. Remarkably, large parts of the Indian Ocean and the Western Pacific, as well as some northern parts in the area of the Antarctic Circumpolar Current ACC (e.g., close to Australia) and individual areas in the Atlantic Ocean (e.g., near the Gulf Stream), evince finally only very small deviations, which indicates a successful scale factor determination in large parts of the ocean. In general, the deviations increase in the Eastern Pacific, the Atlantic, and the Northern and Southern Oceans.

Moreover, the standard deviation of the final factor $\sigma_{\mathbf{k}_f}$, which is considered as associated uncertainty (shown in the upper right of Fig. 4), also exhibits a significant reduction in the oceanic areas. The pattern of this reduced uncertainty correlates well with the high variance of the OIMF (see Fig. 2, right panel). Areas characterized by high variability of the OIMF evince low uncertainties, whereas areas with a tiny OIMF variability evince high uncertainties. Note that the mean of the OIMF does not affect the results of the scale factor determination (Fig. 2, left panel). However, it can be seen

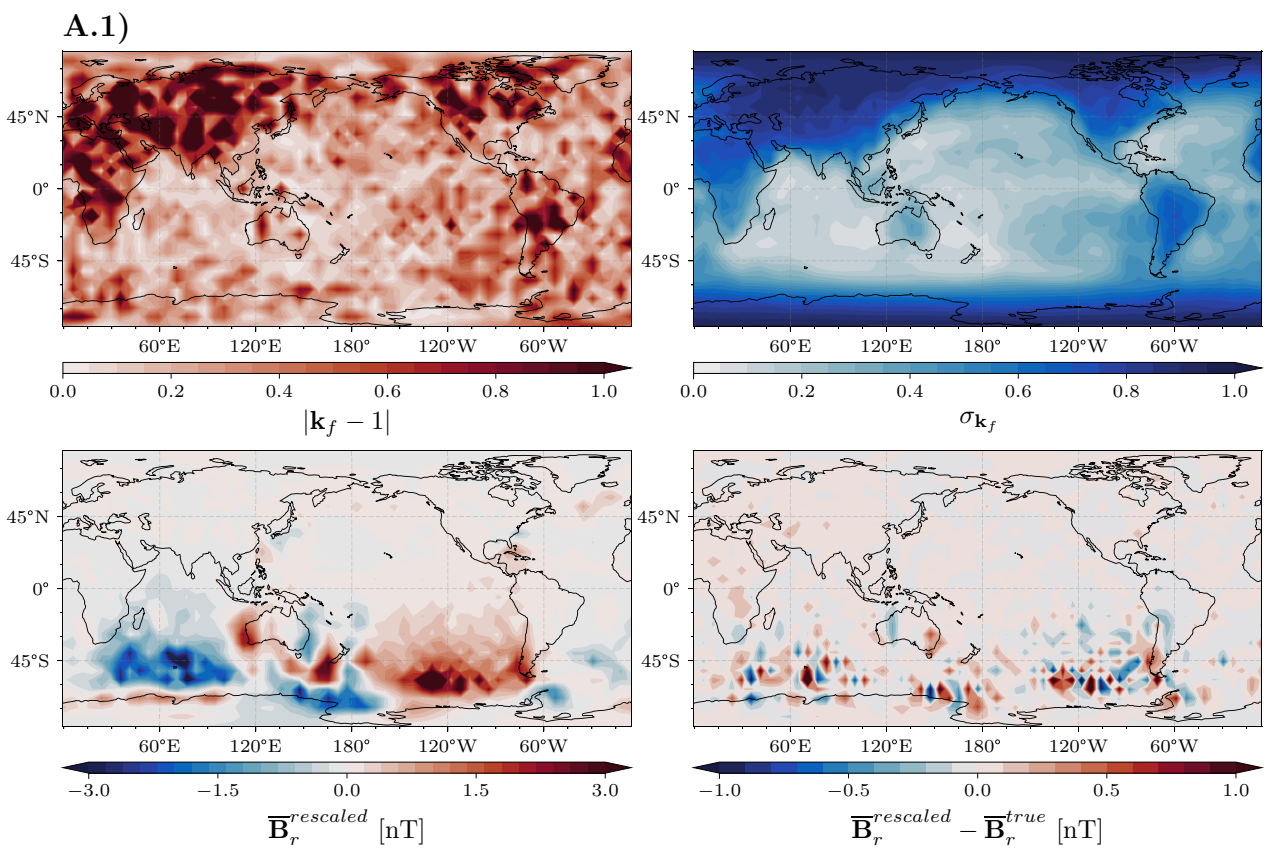

Fig. 4 The assimilation results for the ideal test case scenario with identical true and imposed magnetic fields. The upper plots show both the absolute deviation of the final scale factor $\mathbf{k}_f$ from the true value of 1 (left) and the associated uncertainty (posterior standard deviation) of the final scale factor $\sigma_{\mathbf{k}_f}$ (right). Dark red (respectively, blue) indicates unchanged major deviations (respectively, posterior standard deviation) after the assimilation, whereas lighter colors point out areas with lower deviations and reduced uncertainty. The bottom plots present the results for the rescaled imposed field using the final scale factor. The radial component of the temporal averaged rescaled OIMF $\overline{\mathbf{B}}_r^{\text{rescaled}}$ is shown on the left. Its deviations from the temporal averaged true oceanic contribution $\overline{\mathbf{B}}_r^{\text{true}}$ included in the observations, are shown on the right. Here, red colors indicate higher and blue lower values in the radial component of rescaled OIMF than the true OIMF. Note the different color range to show the deviations

that at higher latitudes (larger than 60°), the standard deviation of the scale factor strongly increases. This latitude dependence is explainable by the fact that the influence of the ionospheric magnetic field contribution also increases strongly at higher latitudes and corresponds to the chosen nighttime data selection below 60°. Overall, regions with small deviations of the scale factor from the true value coincide with areas of low standard deviation of the scale factor, and conversely, larger deviations occur in areas with higher standard deviation. We conclude that the posterior standard deviation of the scale factor is a valuable measure to assess the quality of the assimilated scale factor.

Finally, the bottom plots in Fig. 4 present the mean rescaled OIMF and its deviation from the mean true OIMF included in the observations. As stated before, the rescaled field reflects the detectable part of the OIMF and emphasizes the part of the signal gained from the true OIMF by the assimilation. The mean rescaled field is very similar to the mean of the true OIMF (compare to Fig. 2). The globally slight deviations demonstrate remarkable accordance between the rescaled field and the true oceanic field. The rescaled field is used to calculate the NRMSD at each location (note that in the ideal scenario, the NRMSD is equivalent to $|\mathbf{k}_f - 1|$). In this test case scenario, the averaged NRMSD over the oceans is 0.26 (the grid points over the ocean are again selected using the ETOPO1 dataset). The average $\sigma_{\mathbf{k}_f}$ in the oceanic area is 0.38.

Further insight can be gained by looking at the development of the scale factor over time. The scale factor evolution in two different areas is shown: One area with high and another with relatively low variability of OIMF. The high-variability area is located in the Southern Indian Ocean between Africa and Australia, around 45° South, and the low-variability area is located in the Eastern Pacific close to the coast of central South America, around 15° South (see also Fig. 2). Both the point-wise local results from 10 connected grid points as well as the spatial mean over these areas are presented in Fig. 5. As can be seen from this figure, the factor evolves remarkably fast towards the true value of 1.0. The spatial mean in the high-variability area converges already close to one after less than one year of assimilated data. It is clearly visible that the convergence in the case of the low-variability area takes a longer time. However, the spatial mean in this area also approaches the correct value after approximately two years of assimilated data. In comparison, the spread of the local **k**-results is significantly narrower for the high-variability area, which corresponds well to the lower standard deviation of the scale factor. Promisingly, the fast convergence of the scaling factors emphasizes the method's high sensitivity to magnetic signals from OIMF.

These results confirm the detectability of the OIMF in this ideal test case scenario using assimilation. We deduce that under the condition of imposing the correct OIMF, our proposed method allows the identification of OIMF in geomagnetic satellite observations.

As stated before, the results can be further improved by incorporating an exponentially decaying spatial correlation structure at the beginning of the assimilation. The results of an assimilation (A.2) using such a prior spatial covariance with a correlation length of 2000 km are presented in Fig. 6. As compared to Fig. 4, there is an overall improvement in the scale factor determination. The

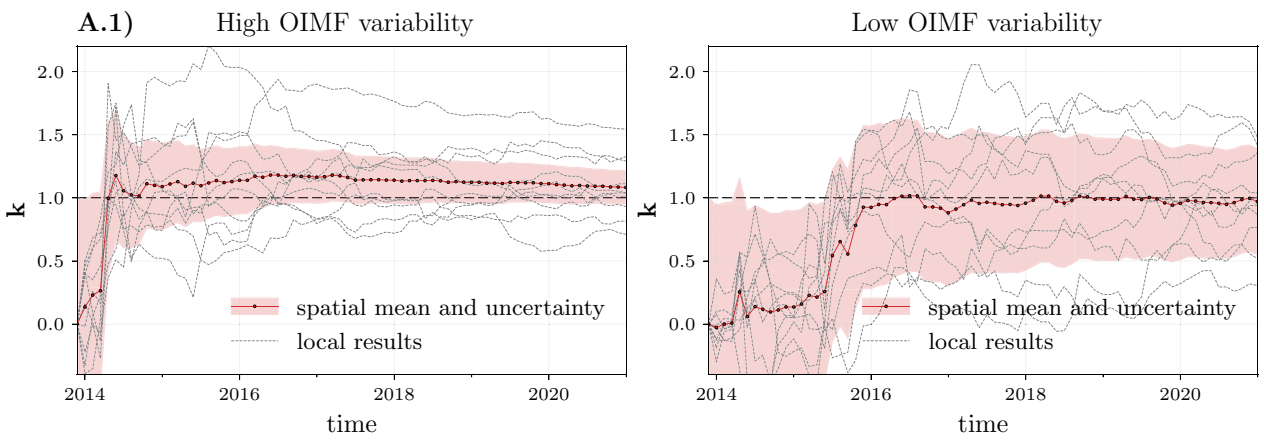

Fig. 5 The evolution of the scale factor over the entire assimilation period. The convergence of the scale factor is considered in two different areas: an area of high OIMF variability located in the Southern Indian Ocean (left side) and an area of low OIMF variability located in the Eastern Pacific (right side). The grey lines denote the point-wise local factors, and the red lines highlight the area's spatial averaged mean and uncertainty (posterior standard deviation). The horizontal, dashed, black line indicates the true scale factor

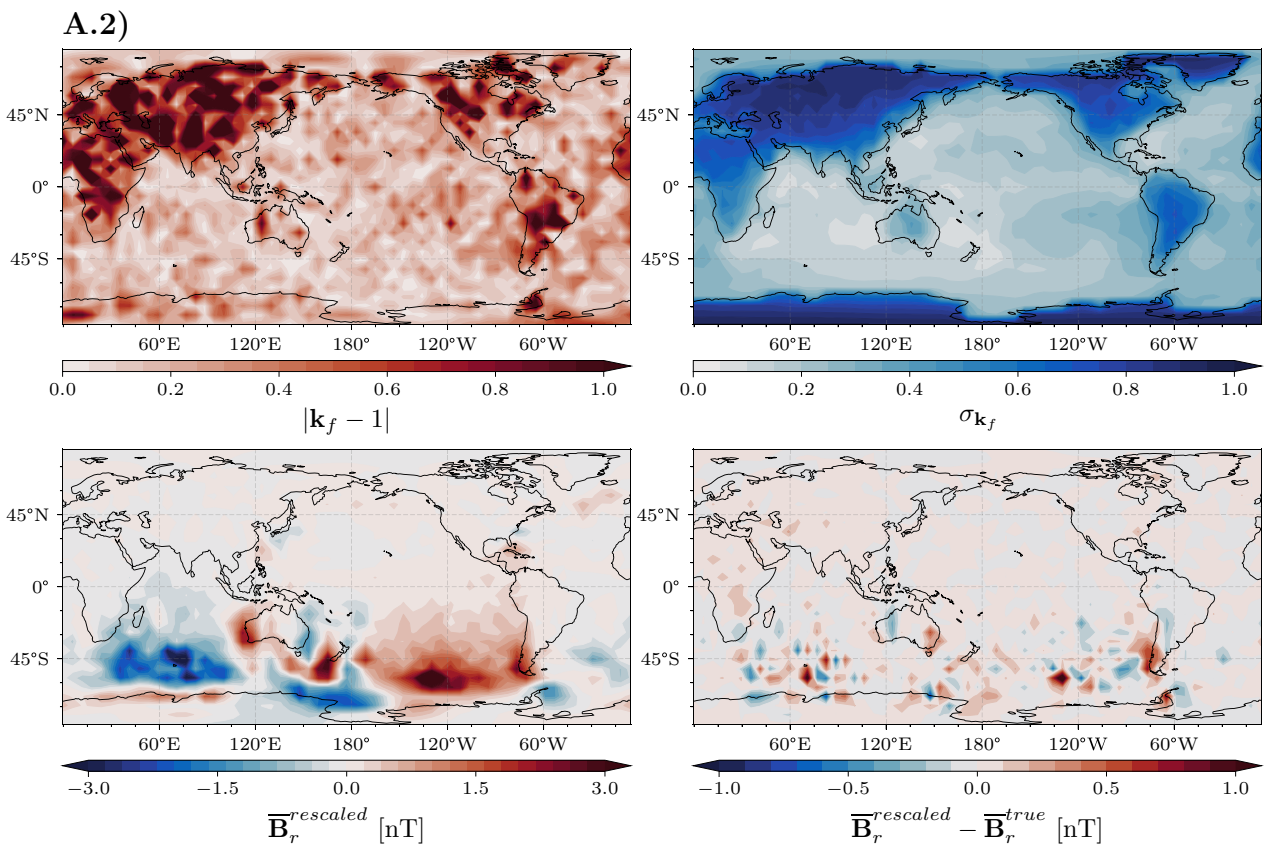

Fig. 6 The improved assimilation results using an additional prior spatial correlation in the case of identical true and imposed magnetic fields. Again, the upper plots show the absolute deviation of the final scale factor $\mathbf{k}_f$ from the true value of 1 on the left and the associated uncertainty (posterior standard deviation) of the final scale factor $\sigma_{\mathbf{k}_f}$ on the right. The bottom plots present the corresponding temporal average of the radial rescaled OIMF $\overline{\mathbf{B}}_r^{\text{rescaled}}$ on the left. And its deviation from the temporal averaged true radial OIMF $\overline{\mathbf{B}}_r^{\text{true}}$ are shown on the right

deviation as well as the standard deviation of the scale factor are further reduced compared to the previous result. Due to the spatial correlation, σ_{k_f} decreased significantly also at latitudes larger than 60°. Furthermore, the improved scale factor determination is also emphasized by the smaller deviations of the rescaled radial magnetic field from the true radial magnetic field (bottom right plot in Fig. 6). Expectantly, the enforced spatial relation between the scale factor at the beginning of the assimilation results in a slightly smoother rescaled radial magnetic field (compare bottom left plots of Fig. 6 and Fig. 4). By looking at the factor evolution in the same areas as chosen before (see Fig. 7), one can clearly see the effect of the type of prior spatial covariance. On the one hand, the spread of the local point-wise results is much narrower according to the lower uncertainty, and on the other hand, the spatial correlation expedites the convergence toward the correct value at the beginning of the assimilation. The overall average over the ocean of the NRMSD decreased from 0.26 before down to 0.17. Correspondingly, the average standard deviation of the scale factor was reduced from 0.38 to 0.22. Thus, we conclude that imposing a priori spatial correlations increases the accuracy of factor determination.

Finally, we used the ideal test case scenario to investigate a little further the influence of the magnetic component resulting from the ionosphere. In general, the Kalmag assimilation distinguishes between internal and external sources. As one of the internal sources, the ionospheric field is arguably a strong competitor for the separation of ocean-induced magnetic fields. In comparison, the other two internal sources from the core and lithosphere differ more clearly in time behavior since they develop much slower. Most of the ionospheric influence is avoided by the selection of nighttime data and low geomagnetic activity. Moreover, the crucial areas of this assimilation are the mid-latitudes (due to the applied data selection below 60° and low ocean-induced signals at the geomagnetic equator). In this case, the solar-quiet magnetic fields dominate the ionospheric component. Since

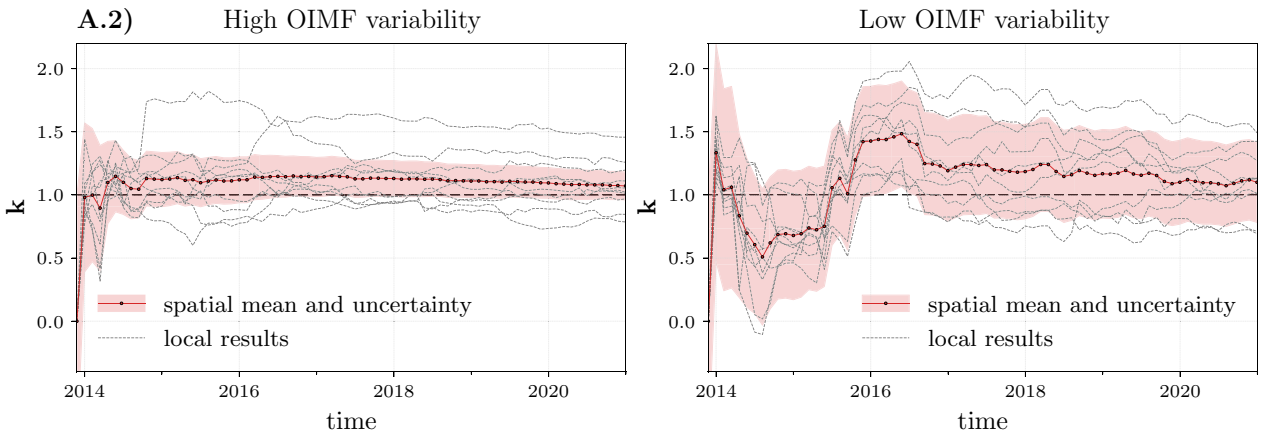

Fig. 7 The scale factor evolution for test case scenario A.2). As in Fig. 5, the evolution is presented over the entire period and for two different areas of high (left) and low (right) variability of the OIMF. Again, both local results (grey) and spatial mean (red) are shown. However, in the assimilation shown here, an exponentially decaying spatial covariance structure is used at the beginning of the assimilation

studies like Suzuki (1978) and Takeda (2002) found that low degrees of SH can capture the solar-quiet fields, we simulated the ionospheric component in our OSSE up to an SH degree of 5 in the first place. However, the treatment of the ionospheric magnetic field still affects the method's sensitivity. Thus, we performed two additional assimilations A.3 to demonstrate possible ionospheric influences. Here, we simulated the ionospheric component and included it in the artificial observations by a much higher spatial resolution of SH 10 and SH 50. The effect on the detectability of the OIMF is illustrated in Fig. 8. Both assimilation results, for the ionosphere up to SH 10 and up to SH 50, show a similar pattern compared to the previous assimilation using the ionosphere up to SH 5 (see Fig. 6). However, the scale factor deviation increases slightly for the SH 10 version and, more significantly, for the SH 50 version, which indicates that the influence of the ionosphere can complicate the separation of the OIMF. Similarly, the associated uncertainty of the factor increases in both cases. Due to the spatially expanded resolution of the ionosphere, the averaged NRMSD over the ocean increased from 0.17 to 0.21 (ionosphere SH 10) and up to 0.29 (ionosphere SH 50). Accordingly, the average standard deviation of the final scale factor increases from 0.22 up to 0.27 (ionosphere SH 10) and 0.43 (ionosphere SH 50). We deduce from these assimilations that the ionosphere can affect the scale factor determination. Probably, this has to be taken into account when applying the method outside of this OSSE. However, one also can conclude from these assimilations that the associated uncertainty of the scale factor covers the influence of other magnetic sources like the ionosphere.

Test case scenario B: deviating true and imposed magnetic field

In this second test case scenario, the imposed oceanic field is not identical anymore to the true oceanic field included in the Swarm-like artificial data. The objective of this test case is to show the robustness and the optimality of the proposed method in the presence of slight deviations between the imposed and true OIMF. To ensure comparability, we left the imposed field the same as in the assimilations before and replaced the true oceanic contribution in the Swarm-like artificial data. In doing so, the results are not affected by differently imposed OIMF variability. We consider two simple types of differences between the imposed and true OIMF: On the one hand, spatial differences, where the true OIMF primarily differs in the spatial domain, and on the other hand, temporal differences, where mainly the temporal behavior of the true OIMF is changed. Of course, this is not strictly distinguishable since the magnetic field is not restricted to a fixed point in space both spatial and temporal differences influence each other. However, each case emphasizes the main cause of the differences.

In order to test the effect of spatial deviations, we investigate spatial oversampling of the true OIMF. Instead of using the same spatial resolution as the imposed OIMF, we included the true OIMF in the artificial satellite data with a higher spatial resolution. Two assimilations are performed in this setup: One with true OIMF with spherical harmonics up to degree 45 (SH 45) and one with up to degree 60 (SH 60). These assimilations mimic the more realistic scenario where the presumed proxies of the OIMF are imposed with lower spatial resolution as the true field. To examine the effect of temporal deviations, we consider a temporally noisy true OIMF. Again

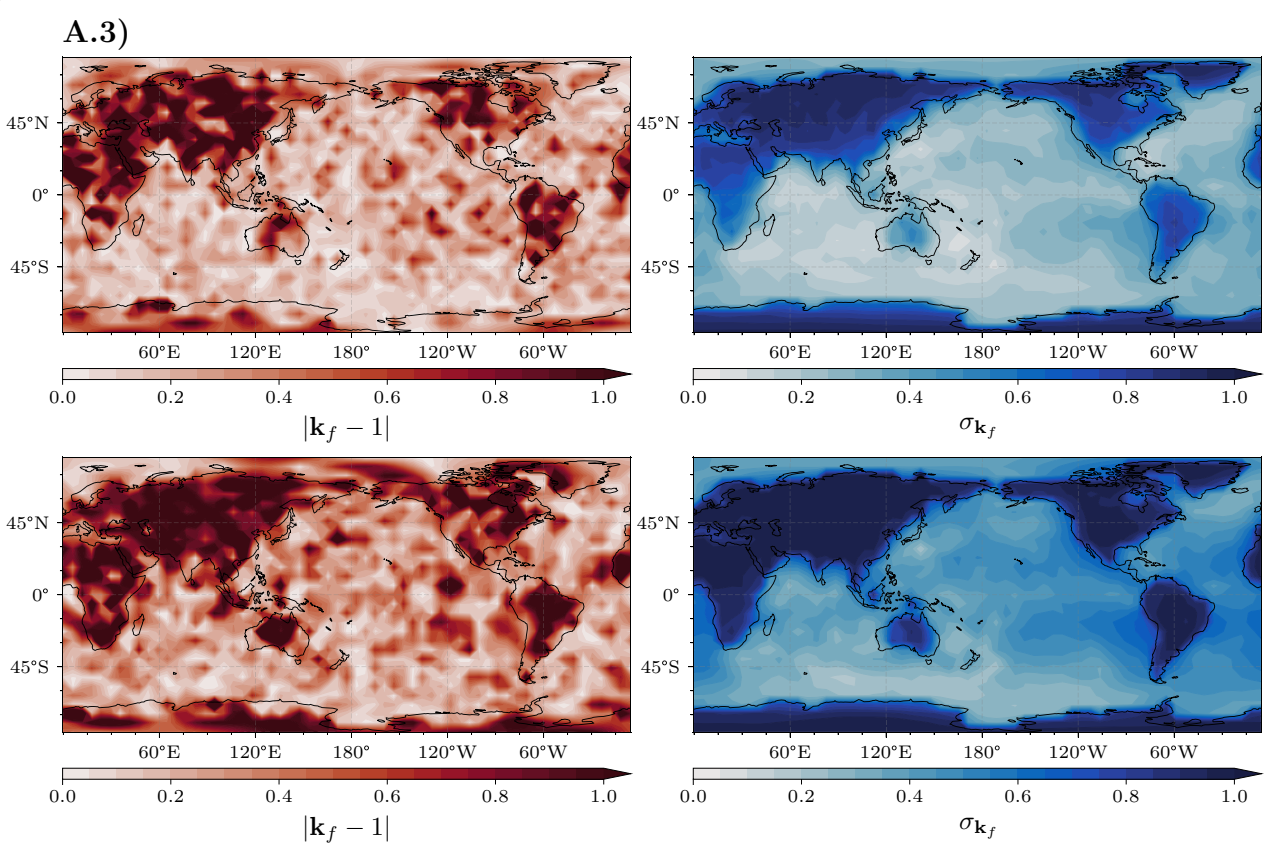

Fig. 8 The assimilation results for the ideal test case scenario, but with an increased spatial resolution of the ionospheric field. The results are obtained using the additional spatial correlation. On the top, the ionospheric component is simulated up to SH 10 and on the bottom up to SH 50. In both cases, the left side presents the absolute deviation to the final scale factor $\mathbf{k}_f$ from the true value of 1, and the associated uncertainty (posterior standard deviation) of the final scale $\sigma_{\mathbf{k}_f}$ is shown on the right side

two further assimilations are studied: one with low-frequency noise (LF noise) and another one with high-frequency noise (HF noise). In both cases, the noise added at each position is randomly drawn from a gaussian distribution with a standard deviation equal to the STD of the true OIMF at the corresponding location. In the case of LF noise, it is added to the SH 30 imposed OIMF every 60 days and interpolated within the interval. However, to create HF noise, the noise is added daily to the SH 30 imposed OIMF. In doing so, the HF noise can be seen as a scenario where daily variations of the OIMF are not covered correctly by the imposed OIMF. In contrast, the LF noise mimics a case where the imposed field misses parts of monthly or longer variations in the true OIMF. The deviations between imposed and true OIMF are exemplarily illustrated in Fig. 9.

The results of all four considered assimilations with differing true OIMF are shown in Fig. 10. The presented results are taken from the improved assimilations using the prior covariance accounting for spatial correlations. Due to the deviations of the imposed and true OIMF, the true value of the scale factor is not precisely one at each location and time step anymore. Therefore, the results are presented directly as NRMSD (Eq. 8) between the rescaled and true OIMF anomalies. We used the magnetic field anomalies for the NRMSD calculation since our method is not sensitive to the mean values. Expectantly, the NRMSD shows the familiar pattern of large values over land and decreased values in oceanic areas. Despite the slightly incorrect imposed OIMF, large parts show significantly reduced NRMSD. Remember, at the beginning of the assimilation, the scale factor is set to zero, which corresponds to an NRMSD of one at each location. Overall, the NRMSD clearly evince more significant deviations for all assimilations compared to the previous ideal scenario (Fig. 6, where the $|\mathbf{k}_f - 1|$ corresponds to the NRMSD). In general, the spatial deviations exhibit a larger NRMSD than the considered temporal deviations. For the temporal deviations, the areas of decreased NRMSD extended more over

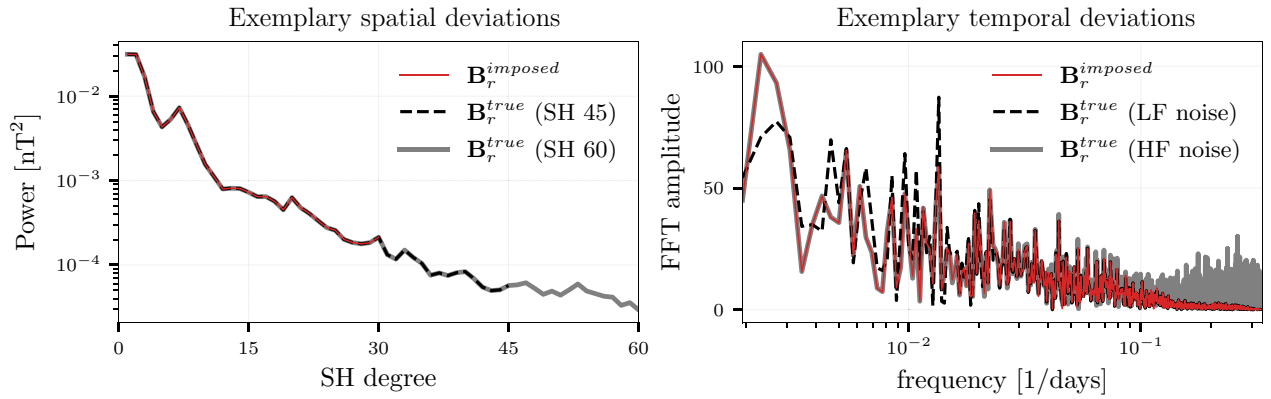

Fig. 9 Exemplary illustration of the spatial and temporal differences between the imposed and true fields studied in test case scenario B. The red line represents the unchanged imposed OIMF (identical to the previous scenario), whereas black and grey denote several different true OIMF used in this test case scenario. On the left, the power spectrum highlights spatial differences between imposed and two deviating true OIMF (shown at a fixed time step). On the right, the frequency spectrum exemplifies temporal differences between the imposed field and two other deviating true OIMF (shown at an exemplary fixed location)

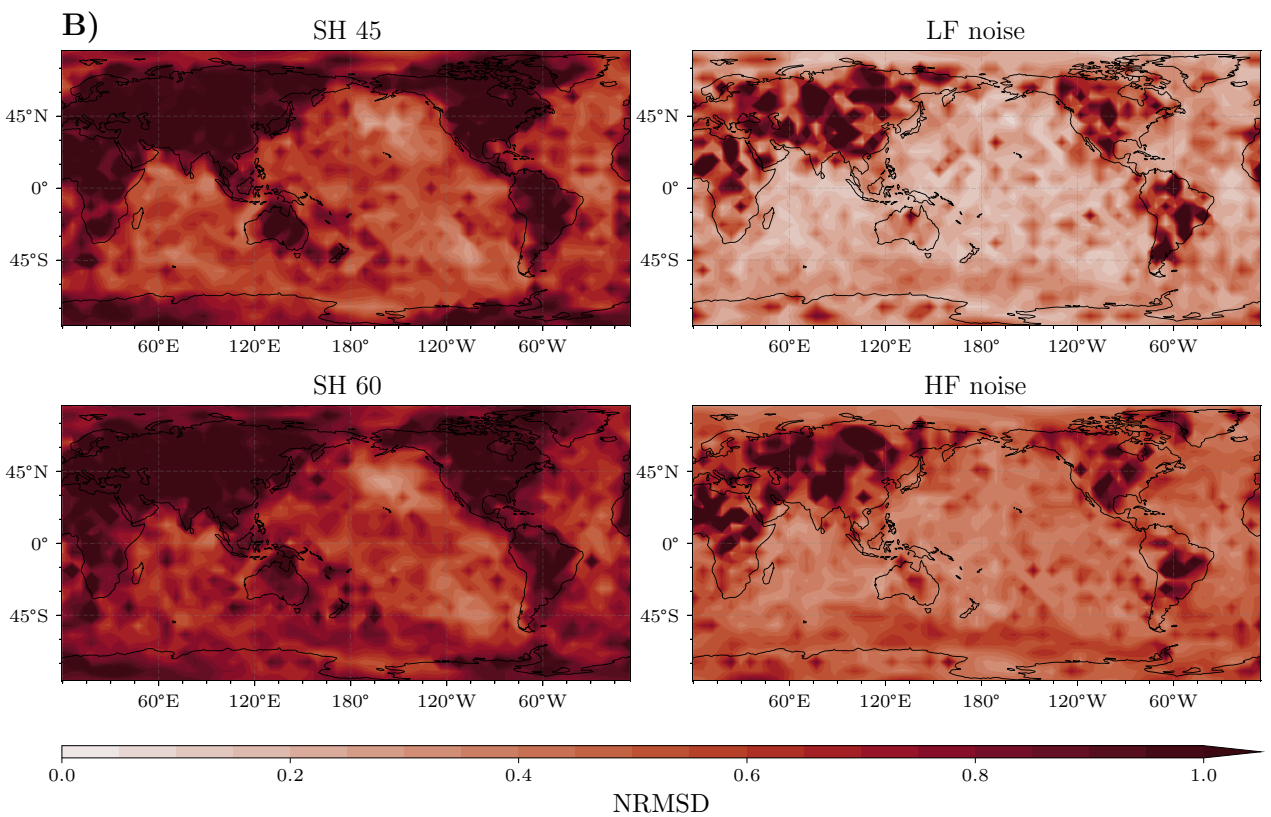

Fig. 10 The assimilation results using various from the imposed field differing true OIMFs. The shown NRMSD expresses how well the rescaled OIMF anomalies reflects the true OIMF anomalies. The left side shows the result for spatial deviations using a true OIMF with SH resolution of degrees 45 and 60. On the right side, temporal deviations in the form of low-frequency (LF) and high-frequency (HF) noise are considered. Dark red indicates areas with large NRMSD and, therefore, a large discrepancy between rescaled and true OIMF; respectively, lighter colors point out areas of good agreement

the entire oceans. The assimilation results using a true OIMF with SH 60 compared to the version using SH 45 have a similar pattern, but the NRMSD gets larger. Likewise, the temporal deviations caused by high-frequency noise show a slightly higher NRSMD than those caused by low-frequency noise. However, when evaluating the results and comparing them to the ideal test case scenario, it must be taken into account that there is already a significant NRMSD between the imposed and the true OIMF. Moreover, it is vague to what extent the scale factor approach generally can correct these imposed deviations. In the context of this OSSE, this can be clarified by calculating a theoretically optimal scale factor for this scenario. At each grid point, this optimal scale factor is determined by a least-square-fit of the time series between the true and the scaled imposed field. In doing so, the optimal factor minimizes the NRMSD between the true and an optimal scaled imposed OIMF anomalies. We considered this optimal factor as the best possible result of the Kalmag assimilation.

We used this factor to illustrate the optimal achievable NRMSD. Exemplary for both the imposed NRMSD (deviation between imposed and true OIMF anomalies), as well as the optimal NRSMD (deviation between optimal rescaled and true OIMF anomalies), is shown for the assimilation using the true OIMF with SH 45 in Fig. 11. From this figure, it can be seen that both strongly coincide with each other. We draw two conclusions from this: First, the imposed deviations in this scenario can hardly be corrected by any scale factor, which also emphasizes a limitation of the scale factor approach. Second, the increased NRMSD compared to the ideal scenario is primarily explainable by the imposed NRMSD. Thus, in this test case scenario, the imposed NRMSD could arguably be considered a lower limit of the achievable NRMSD of the rescaled field. Apart from that, the resulting scale factor from the assimilation is still a measure of detectability and how well the imposed signal can be recovered from the artificial observational data.

Finally, Fig. 12 summarizes the averaged NRMSD of all assimilations considered in test case scenario B and compares them to the imposed NRMSD. This figure underlines, that more significant deviations between the true and the imposed OIMF result in a larger NRMSD between the rescaled and true field after the assimilation (e.g., lower NRMSD for temporal deviations compared to spatial ones). In all cases, the resulting NRMSD after the assimilation is very close to the imposed NRMSD. Moreover, the average imposed NRMSD is within the uncertainty range of the results. We conclude that the proposed method allows a reasonable scale factor determination regardless of slight deviations between the imposed and true OIMF. Furthermore, Fig. 12 presents the assimilation results with and without imposed a priori spatial correlations. This comparison confirms the benefits of accounting for prior spatial correlations, with an averaged NRMSD slightly smaller in all test cases. From Fig. 12, it is also clearly visible that the usage of prior correlations reduces the final uncertainty of the scale factors and the resulting NRMSD, indicating an overall better factor determination.

We summarize from test scenario B that the Kalman filter algorithm determines an appropriate scale factor despite deviations in the presumed proxies. As a result,

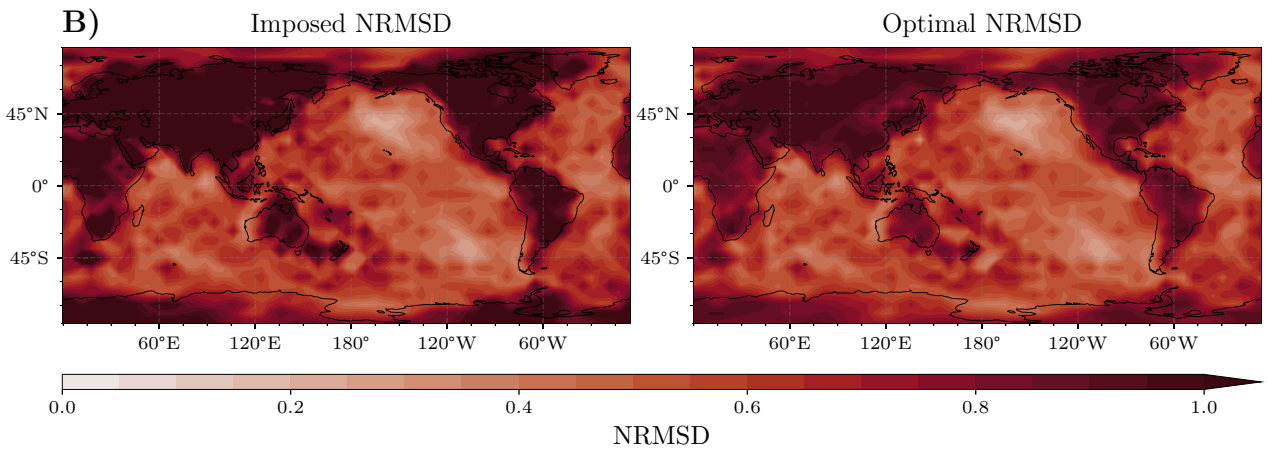

Fig. 11 The original deviations between the true and imposed OIMF anomalies (imposed NRMSD) are shown on the left. The deviations between true and theoretically best possible rescaled OIMF anomalies (optimal NRMSD) are illustrated on the right side. Both are shown exemplarily for the test case using a different true OIMF with a spatial oversampling up to SH 45. Dark colors indicate large discrepancies between the true and imposed (respectively, optimal rescaled) OIMF anomalies, and lighter colors accordingly, a good agreement. Both plots do not rely on assimilation results

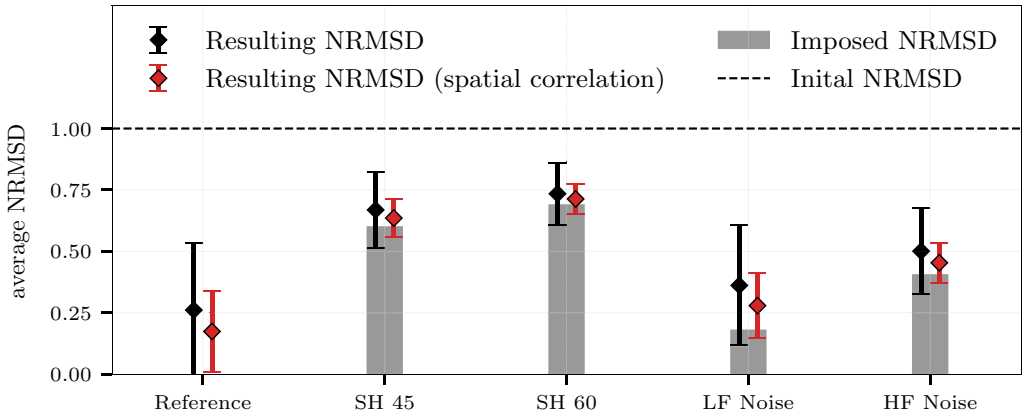

Fig. 12 This plot summarizes the assimilation results of test case scenario B. The NRMSD averaged over the ocean is shown for several cases with deviating true OIMF. The References denote the results from the ideal test case. Both results from assimilation without (black) and with (red) the use of an a priori spatial correlation are shown. The corresponding uncertainty resulting from the posterior STD of the scale factor is indicated as well. As a comparison, the imposed NRMSD (deviations between imposed and true OIMF anomalies) are marked in grey. These indicate the best achievable results and are considered a lower limit of possible improvements

the final rescaled OIMF reflects the true OIMF as comparably good as the imposed one. Consequently, larger deviations in the presumed proxies result in a poorer correspondence between rescaled and true OIMF. Apart from that, the results indicate robustness to all sources of deviations (different spatial resolutions as well as low and high-frequency noise). Lastly, the posterior standard deviation proves to be a suitable measure for the uncertainty again, and the use of a prior correlation information improves the results in all cases.

Test case scenario C: deviating conductivity of the imposed magnetic field

This last test case scenario demonstrates a possible application of the presented method and is used further to explore the limitations of the scale factor approach. Moreover, this scenario provides an outlook on how the scale factor can find possible use beyond its measure of detectability.

Again, we examine deviations between the true and imposed fields. We kept the artificial observations the same as in the ideal scenario. However, this time, we slightly changed the presumed proxies by using a different ocean conductivity for their calculations. Instead of deriving the ocean conductivity from the ECCO2 model, we took the annual mean conductivity from the World Ocean Atlas 2018 (WOA18) dataset (Tyler et al. 2017). We chose the 3D ocean conductivity version with a spatial resolution of 1° and adapted it to the vertical layers of the ECCO2 velocities. All other calculation steps remained unchanged. Thus, the imposed OIMF deviates from the true OIMF only due to the different ocean conductivity. The assimilation is then performed like in the previous test case scenario using prior spatial correlations. The results of this assimilation are present in Fig. 13 as NRMSD of the rescaled and the true OIMF anomalies and the associated uncertainty of the scale factor. Clearly, the NRMSD (top left plot in Fig. 13) is decreased over the oceanic areas but, in general, more extensive compared to the ideal test case scenario (see Fig. 6). However, the low uncertainty of the scale factor (top right plot in Fig. 13) indicates an appropriate scale factor determination over the oceanic areas in this test case scenario.

Eventually, we used this test case scenario to investigate if the presumed proxies assuming a different conductivity could be corrected by assimilating artificial observational data. In this case, the deviations of the imposed field should be reduced by the determined scale factor. Therefore, the differences between the imposed NRMSD (between true and imposed OIMF anomalies) and the rescaled NRMSD (between true and rescaled OIMF anomalies) are considered. This is shown as assimilation improvement in Fig. 13 (bottom left plot). The figure points out areas (marked in red) where the rescaled OIMF anomalies are in better accordance with the true OIMF anomalies than the imposed ones. At these locations (e.g., along the East Asian coast, the Gulf of Mexico, southeast of Australia, and southwest of Africa), the imposed OIMF anomalies are adequately corrected by the scale factor resulting from the assimilation. On the downside, in some areas (marked in blue), the imposed OIMF anomalies could not be improved through the scale factor. However, especially over land, it is not expected to obtain such a scale factor from the assimilation (note again that the assimilation initially assumes a

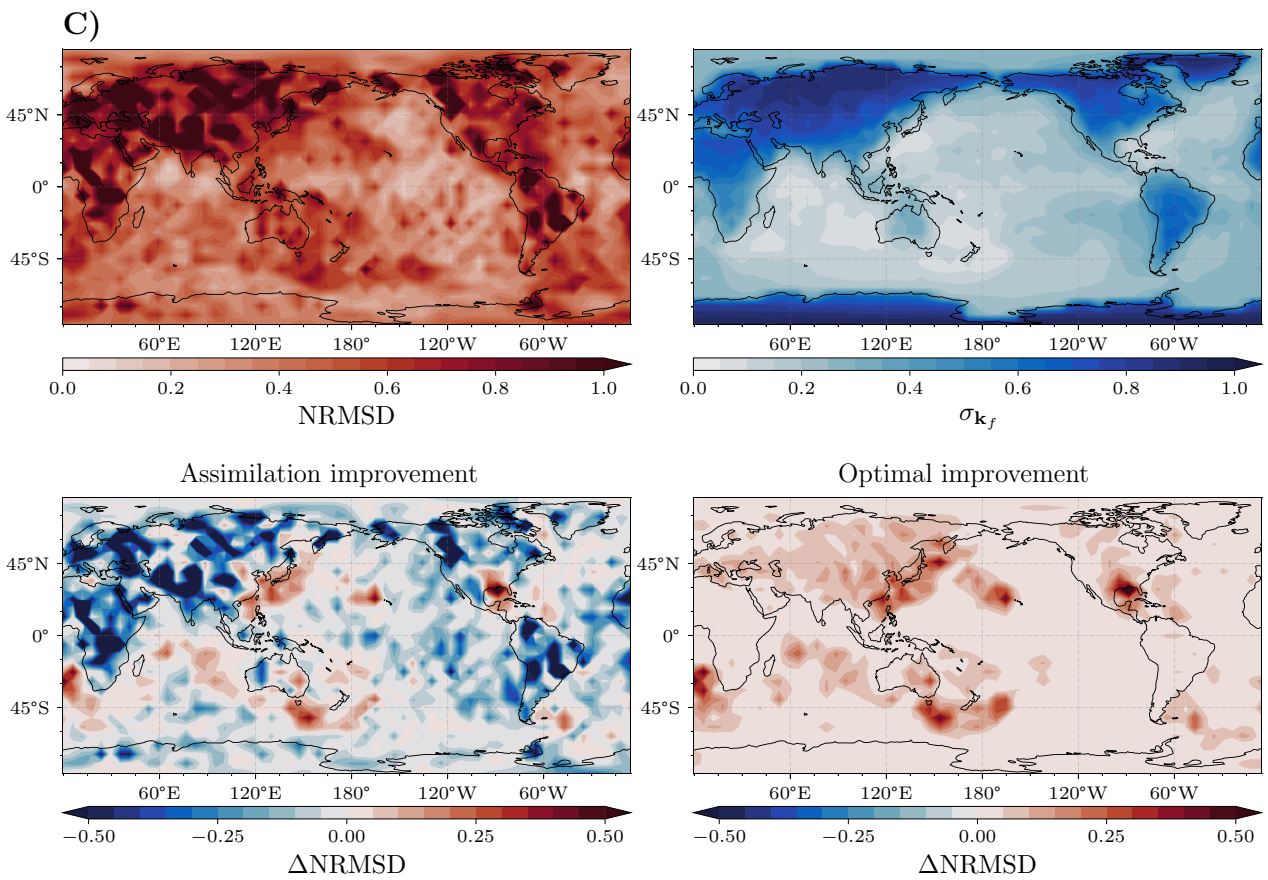

Fig. 13 The assimilation results using an imposed OIMF based on a different ocean conductivity. The top left plot shows the final NRMSD between the rescaled and true OIMF anomalies, and in the top right, the corresponding uncertainty of the determined scale factor is shown. In the bottom left, the assimilation improvement demonstrates how the imposed deviations are changed through assimilation (presented as the difference between imposed NRMSD and rescaled NRMSD). As a comparison, the bottom right plot shows the best possible improvement by an optimal scaling

scale factor of zero). To better evaluate these assimilation improvements, we compare them again with a theoretical optimal scaling of the imposed OIMF. For this purpose, an optimal factor was calculated as described in the previous section to identify the best possible effect due to a scale factor correction. As before, the optimal improvement is described as the difference between the imposed NRMSD and the optimal rescaled NRMSD, indicating how much the imposed deviations can be reduced by optimal rescaling. This optimal improvement is presented in Fig. 13 (bottom right plot). In large areas, the best possible improvement is close to zero, which implies that even an optimal scale factor cannot correct the imposed deviations. But remarkably, the areas of significant improvement through optimal rescaling coincide exceptionally well with the pattern of improvement through assimilation. Additionally, oceanic areas where no improvement could be achieved by assimilation overlap with areas in which also an optimal factor does not lead to any improvement. This evaluation once again demonstrates the optimality of the scale factor determination. We conclude from this test case scenario that the assimilation results in a reasonable scale factor and that its application can possibly be used to obtain valuable information from observational data in the future.

On the applicability to real observations

With regard to the application of the method on real Swarm satellite data, we compared artificial satellite magnetometer data used in the presented OSSE with the real observations from the Swarm satellite mission. Therefore, we subtracted the core and lithosphere components of the Kalmag model from both datasets. The comparison of the remaining magnetic field measurements is presented in Fig. 14 exemplary for the year 2014. The residuals of all three vector components (B_r, B_θ, B_ϕ) of each 100th measurement are shown in dependence on the satellite latitude position. On the one hand, the comparison

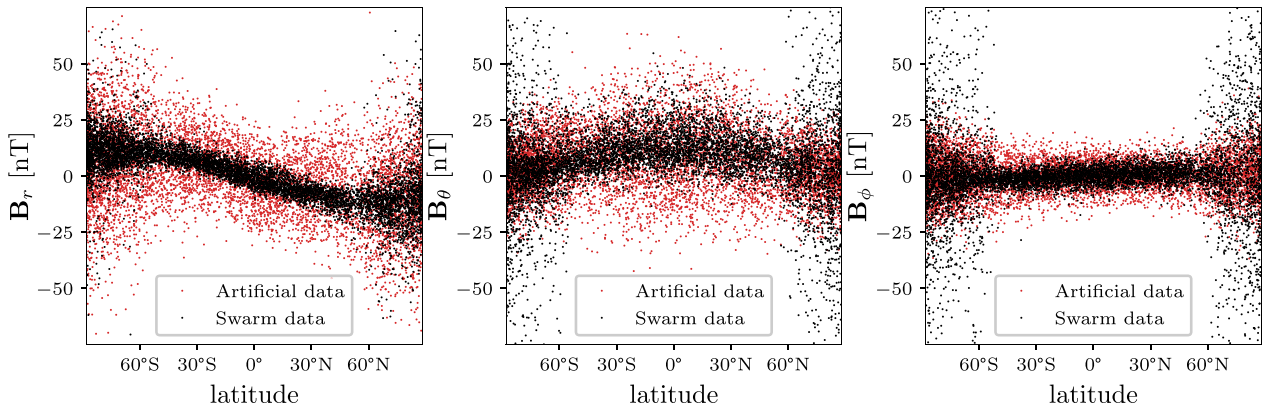

Fig. 14 Comparison of the selected (nighttime and geomagnetic low activity) vector field magnetic satellite measurements. The residuals from the core and lithosphere component are shown. The artificial data used in the presented OSSE are marked in red; the real Swarm observational data are marked in black. All three vector field components (B_r, B_θ, B_ϕ) are shown for each 100th satellite measurement of year 2014 in dependence on the satellite latitude position

shows that the residuals of both artificial and Swarm magnetic field measurements are in the same order of magnitude and similar shape. On the other hand, Fig. 14 discloses differences between the artificial and the real Swarm measurements. The variability of the residuals in the artificial data, especially in the radial component, is larger around the equator and lower than than the variability in the Swarm observations at higher latitudes in the theta and phi components. The lower variability in the higher latitudes of the non-radial components could be well explained by missing field-aligned currents, which are not considered when building the synthetic data set. The increased variability of the artificial data residuals at lower latitudes, particularly the radial component, could indicate an overestimation in the prior of the ionosphere component around the equator. Even though Baerenzung et al. (2022) demonstrated that the ionosphere-induced magnetic source of the Kalmag model is consistent within induction processes, the deviations that occurred between the artificial and the real Swarm satellite data may require further investigation.

Apart from the differences between the artificial and the real Swarm data, another issue arises when it comes to application on real data. In contrast to the OSSE discussed in this paper the induced magnetic signal contained in the real satellite data is not known a priori. Although the analysis of the proposed method indicated a certain robustness and a reasonable scale factor determination, the results of this paper rely purely on the ECCO2 transport estimations. Consequently, the imposed signals and the signals included in the artificial measurements are still based on the same model. However, the oceanic transport predictions and, therefore, the OIMF anomalies may vary more widely. A potential incompatibility of the imposed and the real signal in the Swarm satellite data could affect the assimilation and scale factor determination to a larger extent. Towards the application of the presented method on real Swarm data, the authors propose to expand the variety of imposed magnetic fields and analyze potentially larger incompatibilities by taking into account also different ocean models or observational data.

Conclusion and outlook

This paper presented a method to possibly detect ocean-induced magnetic field (OIMF) signals from general ocean circulation for the first time. The challenging task is the separation of these oceanic signals from other magnetic field components in space-borne observations. The central idea of our new method is to impose the temporal behavior of the ocean circulation component and determine local scale factors using a Kalman filter-based assimilation. As a result, the access to uncertainties due to the Bayesian inversion is of particular value. We introduced our approach with an observing system simulation experiment (OSSE) of different test case scenarios. Firstly, we managed to verify the proposed method in an ideal setup. We were able to show that it is possible to determine a scale factor for an imposed magnetic field regardless the complex temporal behavior and the low intensity of the magnetic field from ocean circulation. The scale factors indicate a detectability of the ocean-induced magnetic field over most areas of the oceans. The method's sensitivity proves to be sufficient for a factor determination within the considered period of 7.1 years of assimilated data. The results of the OSSE also served to point out the main dependencies on the variability of the oceanic magnetic signal and on latitude. Additionally,

we could demonstrate that a priori imposing spatial correlations between the factors further improves the assimilation results significantly. Subsequently, we performed the assimilation in a non-ideal scenario to investigate the effect of spatial and temporal differences of the imposed proxies. This scenario proved the method's robustness in determining a reasonable scale factor and showed the optimality within the scale factor approach. Finally, a third test case scenario presented a possible application, where we could demonstrate that the assimilation can slightly correct imposed proxies, which are based on a differing ocean conductivity. In the end, we compared the artificial data used in the OSSE with the actual Swarm observations regarding the method's application on real geomagnetic satellite observations. Thereby, we discussed potential issues and further investigations to retrieve the magnetic signals induced by ocean circulation from original observations. Extracting a local scale factor of magnetic ocean circulation signals from satellite data would offer plenty of possibilities for gainful utilization. Depending on the imposed field, an analysis of the scale factor itself could contain information about oceanic quantities, like sea water conductivity. Notably, we used only the ECCO2 model to derive the presumed proxies of the OIMF for our method. Further studies could compare this to other ocean models, multi-observational ocean products like ARMOR3D (Guinehut et al. 2012; Mulet et al. 2012), or estimates from sea surface height, like suggested by Saynisch et al. (2018). Since our method only relies on the temporal behavior of magnetic field estimations and even provides uncertainties, this would create a new observational source of information. Potentially, the rescaled ocean-induced magnetic field from circulation may also serve as input for assimilation experiments regarding ocean circulation models, such as Irrgang et al. (2017). Particularly, in the light of further possible upcoming magnetic field missions like NanoMagSat (Hulot et al. 2018), detecting ocean-induced signals from circulation continues to be of high interest.

Abbreviations

ACC: Antarctic Circumpolar Current; ECCO2: Estimating the Circulation and Climate of the Ocean, Phase II project; ETOPO: The ETOPO1 Global Relief Model; IGRF-13: International Geomagnetic Reference Field, 13th generation; OGCM: Ocean General Circulation Model; OIMF: Ocean-Induced Magnetic Field; OSSE: Observing System Simulation Experiment; NRMSD: Normalized root mean square deviation; SH: Spherical harmonic functions; STD: Standard deviation; TEOS-10: Thermodynamic Equation of Seawater 2010; WOA18: World Ocean Atlas 2018; X3DG: 3D Electromagnetic Induction Solver.

Acknowledgements

The authors gratefully acknowledge the opportunity to use the data from the ECCO2 ocean model, the IGRF-13 geomagnetic reference field, and the Swarm satellite mission. We directed special thanks to Alexey Kuvshinov (kuvshinov@erdw.ethz.ch) for the opportunity to use the 3D electromagnetic induction solver X3DG.

Author contributions

AH conducted the OSSE and was the major contributor in writing the manuscript. JS and CI participated in the design of the OSSE and supervised the study. JB developed the Kalmag code and implemented the additional magnetic source for ocean circulation. MT is involved with acquisition of funding and administration of the project. All authors read and approved the final manuscript.

Funding

Open Access funding enabled and organized by Projekt DEAL. This study was funded by the German Research Foundation (SPP1788, Dynamic Earth) and the Initiative and Networking Fund of the Helmholtz Association through the project "Advanced Earth System Modelling Capacity (ESM).

Availability of data and materials

The dataset of the ECCO2 ocean model used in the current study are available at: https://ecco.jpl.nasa.gov/drive/files/ECCO2/cube92_latlon_quart_90S90N. The used additional material for the sediment conductance can be downloaded at: https://igppweb.ucsd.edu/~gabi/sediment.html#ftp. The mantel conductivity from Alexander Grayver is available at: https://github.com/agrayver/ConductivityProfile. The dataset of the WOA18 ocean conductivity can be found: https://www.ncei.noaa.gov/access/world-ocean-atlas-2018/. The data of the Earth's main magnetic field from the IGRF-13 are available at: https://www.ngdc.noaa.gov/IAGA/vmod/igrf.html. The Swarm satellite magnetometer data can be downloaded from: ftp://swarm-diss.eo.esa.int/Level1b/Entire_mission_data/MAGx_LR/. The K_p index can be downloaded from: ftp://ftp.gfz-potsdam.de/pub/home/obs/kp-ap/. The geomagnetic field model Kalmag can be found: https://ionocovar.agnld.uni-potsdam.de/Kalmag/. The extended Kalmag assimilation presented here is available from the corresponding author on reasonable request.

Declarations

Competing interests

The authors declare that they have no competing interests.

Author details

[1]Helmholtz Centre Potsdam, GFZ German Research Centre for Geosciences, Section 1.3: Earth System Modelling, Potsdam, Germany. [2]Institute of Meteorology, Freie Universität Berlin, Berlin, Germany.

Received: 16 May 2022 Accepted: 10 November 2022
Published online: 09 December 2022

References

Alken P, Thébault E, Beggan CD, Amit H, Aubert J, Baerenzung J, Bondar TN, Brown WJ, Califf S, Chambodut A, Chulliat A, Cox GA, Finlay CC, Fournier A, Gillet N, Grayver A, Hammer MD, Holschneider M, Huder L, Hulot G, Jager T, Kloss C, Korte M, Kuang W, Kuvshinov A, Langlais B, Léger J-M, Lesur V, Livermore PW, Lowes FJ, Macmillan S, Magnes W, Mandea M, Marsal S, Matzka J, Metman MC, Minami T, Morschhauser A, Mound JE, Nair M, Nakano S, Olsen N, Pavón-Carrasco FJ, Petrov VG, Ropp G, Rother M, Sabaka TJ, Sanchez S, Saturnino D, Schnepf NR, Shen X, Stolle C, Tangborn A, Tøffner-Clausen L, Toh H, Torta JM, Varner J, Vervelidou F, Vigneron P, Wardinski I, Wicht J, Woods A, Yang Y, Zeren Z, Zhou B (2021) International geomagnetic reference field: the thirteenth generation. Earth Planets Space 73(1):49. https://doi.org/10.1186/s40623-020-01288-x

Amante C, Eakins B (2009) ETOPO1 1 arc-minute global relief model: procedures, data sources and analysis. NOAA Technical Memorandum NESDIS NGDC-24. National Geophysical Data Center, Boulder, Colorado

Baerenzung J, Holschneider M, Wicht J, Lesur V, Sanchez S (2020) The Kalmag model as a candidate for IGRF-13. Earth Planets Space 72(1):163. https://doi.org/10.1186/s40623-020-01295-y

Baerenzung J, Holschneider M, Saynisch-Wagner J, Thomas M (2022) Kalmag: a high spatio-temporal model of the geomagnetic field. Earth Planets Space 74(1):139. https://doi.org/10.1186/s40623-022-01692-5

Bao S, Wang H, Ren Z, Yan H, Chen J (2020) Spatial and temporal scales of sea surface salinity in the tropical Indian Ocean from SMOS, Aquarius and SMAP. J Oceanogr 76(5):389–400
Brankart J-M, Cosme E, Testut C-E, Brasseur P, Verron J (2010) Efficient adaptive error parameterizations for square root or ensemble kalman filters: application to the control of ocean mesoscale signals. Monthly Weather Rev 138(3):932–950
Dostal J, Martinec Z, Thomas M (2012) The modelling of the toroidal magnetic field induced by tidal ocean circulation. Geophys J Int 189(2):782–798
Everett ME, Constable S, Constable CG (2003) Effects of near-surface conductance on global satellite induction responses. Geophys J Int 153(1):277–286
Flosadottir AH, Larsen JC, Smith JT (1997) Motional induction in North Atlantic circulation models. J Geophys Res Oceans 102(C5):10353–10372
Grayver AV, Schnepf NR, Kuvshinov AV, Sabaka TJ, Manoj C, Olsen N (2016) Satellite tidal magnetic signals constrain oceanic lithosphere–asthenosphere boundary. Sci Adv 2(9):e1600798
Grayver A, Munch F, Kuvshinov A, Khan A, Sabaka T, Tøffner-Clausen L (2017) Joint inversion of satellite-detected tidal and magnetospheric signals constrains electrical conductivity and water content of the upper mantle and transition zone: inversion of satellite magnetic data. Geophys Res Lett 44(12):6074–6081
Guinehut S, Dhomps A-L, Larnicol G, Le Traon P-Y (2012) High resolution 3-D temperature and salinity fields derived from in situ and satellite observations. Ocean Sci 8(5):845–857
Hulot G, Léger J-M, Vigneron P, Jager T, Bertrand F, Coïsson P, Deram P, Boness A, Tomasini L, Faure B (2018) Nanosatellite high-precision magnetic missions enabled by advances in a stand-alone scalar/vector absolute magnetometer. In: IGARSS 2018–2018 IEEE international geoscience and remote sensing symposium, pp 6320–6323
Irrgang C, Saynisch J, Thomas M (2016) Impact of variable seawater conductivity on motional induction simulated with an ocean general circulation model. Ocean Sci 12(1):129–136
Irrgang C, Saynisch J, Thomas M (2017) Utilizing oceanic electromagnetic induction to constrain an ocean general circulation model: a data assimilation twin experiment. J Adv Modeling Earth Syst 9(3):1703–1720
Irrgang C, Saynisch-Wagner J, Thomas M (2018) Depth of origin of ocean-circulation-induced magnetic signals. Annales Geophysicae 36(1):167–180
Irrgang C, Saynisch J, Thomas M (2019) Estimating global ocean heat content from tidal magnetic satellite observations. Sci Rep 9(1):7893
Kelbert A, Kuvshinov A, Velímský J, Koyama T, Ribaudo J, Sun J, Martinec Z, Weiss CJ (2014) Global 3-D electromagnetic forward modelling: a benchmark study. Geophys J Int 197(2):785–814
Kuvshinov A (2008) 3-D global induction in the oceans and solid earth: recent progress in modeling magnetic and electric fields from sources of magnetospheric, ionospheric and oceanic origin. Surv Geophys 29(2):139–186
Larsen JC (1968) Electric and magnetic fields induced by deep sea tides. Geophys J Int 16(1):47–70
Laske G, Masters G (1997) A global digital map of sediment thickness. EOS Trans AGU 78:F483
Manoj C, Kuvshinov A, Maus S, Lühr H (2006) Ocean circulation generated magnetic signals. Earth Planets Space 58(4):429–437. https://doi.org/10.1186/BF03351939
Mazloff MR, Cornuelle BD, Gille ST, Verdy A (2018) Correlation lengths for estimating the large-scale carbon and heat content of the southern ocean. J Geophys Res Oceans 123(2):883–901
McDougall TJ, Barker PM (2011) Getting started with TEOS-10 and the Gibbs seawater (GSW) oceanographic toolbox. SCOR/IAPSO WG127. p 28
Menemenlis D, Fukumori I, Lee T (2005) Using Green's functions to calibrate an ocean general circulation model. Mon Weather Rev 133(5):1224–1240
Menemenlis D, Campin J-M, Heimbach P, Hill C, Lee T, Nguyen A, Schodlok M, Zhang H (2008) ECCO2: high resolution global ocean and sea ice data synthesis. In: AGU fall meeting abstracts. pp OS31C-1292
Mulet S, Rio M-H, Mignot A, Guinehut S, Morrow R (2012) A new estimate of the global 3D geostrophic ocean circulation based on satellite data and in-situ measurements. Deep Sea Res Part II Top Stud Oceanogr 77–80:70–81
Park S-Y, Dash UK, Yu J (2022) Length scale analyses of background error covariances for EnKF and EnSRF data assimilation. Atmosphere 13(2):160
Petereit J, Saynisch J, Irrgang C, Weber T, Thomas M (2018) Electromagnetic characteristics of ENSO. Ocean Sci 14(3):515–524
Sabaka TJ, Tyler RH, Olsen N (2016) Extracting ocean-generated tidal magnetic signals from Swarm data through satellite gradiometry. Geophys Res Lett 43(7):3237–3245
Sabaka TJ, Tøffner-Clausen L, Olsen N, Finlay CC (2018) A comprehensive model of Earth's magnetic field determined from 4 years of Swarm satellite observations. Earth Planets Space 70(1):130. https://doi.org/10.1186/s40623-018-0896-3
Sabaka TJ, Tøffner-Clausen L, Olsen N, Finlay CC (2020) CM6: a comprehensive geomagnetic field model derived from both CHAMP and Swarm satellite observations. Earth Planets Space 72(1):80. https://doi.org/10.1186/s40623-020-01210-5
Šachl L, Martinec Z, Velímský J, Irrgang C, Petereit J, Saynisch J, Einšpigel D, Schnepf NR (2019) Modelling of electromagnetic signatures of global ocean circulation: physical approximations and numerical issues. Earth Planets Space 71(1):58. https://doi.org/10.1186/s40623-019-1033-7
Sanford TB (1971) Motionally induced electric and magnetic fields in the sea. J Geophys Res 76(15):3476–3492
Saynisch J, Petereit J, Irrgang C, Kuvshinov A, Thomas M (2016) Impact of climate variability on the tidal oceanic magnetic signal—a model based sensitivity study. J Geophys Res Oceans 121(8):5931–5941
Saynisch J, Irrgang C, Thomas M (2018) On the use of satellite altimetry to detect ocean circulation's magnetic signals. J Geophys Res Oceans 123(3):2305–2314
Saynisch-Wagner J, Baerenzung J, Hornschild A, Irrgang C, Thomas M (2021) Tide-induced magnetic signals and their errors derived from CHAMP and Swarm satellite magnetometer observations. Earth Planets Space 73(1):234. https://doi.org/10.1186/s40623-021-01557-3
Schnepf NR, Manoj C, Kuvshinov A, Toh H, Maus S (2014) Tidal signals in ocean-bottom magnetic measurements of the Northwestern Pacific: observation versus prediction. Geophys J Int 198(2):1096–1110
Schnepf N, Kuvshinov A, Sabaka T (2015) Can we probe the conductivity of the lithosphere and upper mantle using satellite tidal magnetic signals? Geophys Res Lett 42(9):3233–3239
Stephenson D, Bryan K (1992) Large-scale electric and magnetic fields generated by the oceans. J Geophys Res Oceans 97(C10):15467–15480
Suzuki A (1978) Geomagnetic Sq field at successive universal times. J Atmos Terr Phys 40(4):449–463
Takeda M (2002) Features of global geomagnetic Sq field from 1980 to 1990. J Geophys Res Space Phys 107(A9):SIA 4-1-SIA 4-8
Tyler RH, Mysak LA, Oberhuber JM (1997) Electromagnetic fields generated by a three dimensional global ocean circulation. J Geophys Res Oceans 102(C3):5531–5551
Tyler RH, Maus S, Luhr H (2003) Satellite observations of magnetic fields due to ocean tidal flow. Science 299(5604):239–241
Tyler RH, Boyer TP, Minami T, Zweng MM, Reagan JR (2017) Electrical conductivity of the global ocean. Earth Planets Space 69(1):156. https://doi.org/10.1186/s40623-017-0739-7
Vivier F, Maier-Reimer E, Tyler RH (2004) Simulations of magnetic fields generated by the Antarctic circumpolar current at satellite altitude: can geomagnetic measurements be used to monitor the flow? Geophys Res Lett 31(10):L10306
Wieczorek M, Meschede M (2018) SHTools: tools for working with spherical harmonics. Geochem Geophys Geosyst 19(8):2574–2592

Publisher's Note